# Near-Ideal Optical Metamaterial Absorbers with Super-Octave Bandwidth

**Jeremy A. Bossard,[†] Lan Lin,[†] Seokho Yun, Liu Liu, Douglas H. Werner,[*] and Theresa S. Mayer[*]**

Department of Electrical Engineering, Penn State University, University Park, Pennsylvania 16802, United States. [†]These authors contributed equally to this work.

**ABSTRACT** Nanostructured optical coatings with tailored spectral absorption properties are of interest for a wide range of applications such as spectroscopy, emissivity control, and solar energy harvesting. Optical metamaterial absorbers have been demonstrated with a variety of customized single band, multiple band, polarization, and angular configurations. However, metamaterials that provide near unity absorptivity with super-octave bandwidth over a specified optical wavelength range have not yet been demonstrated experimentally. Here, we show a broadband, polarization-insensitive metamaterial with greater than 98% measured average absorptivity that is maintained over a wide ±45° field-of-view for mid-infrared wavelengths between 1.77 and 4.81 μm. The nearly ideal absorption is realized by using a genetic algorithm to identify the geometry of a single-layer metal nanostructure array that excites multiple overlapping electric resonances with high optical loss across greater than an octave bandwidth. The response is optimized by substituting palladium for gold to increase the infrared metallic loss and by introducing a dielectric superstrate to suppress reflection over the entire band. This demonstration advances the state-of-the-art in high-performance broadband metamaterial absorbers that can be reliably fabricated using a single patterned layer of metal nanostructures.

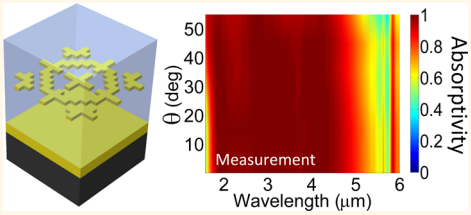


**KEYWORDS:** metamaterial absorber · electromagnetic band gap metamaterial · broadband · optical · infrared · nanoresonator · nanostructure array · emissivity control · enhanced absorption

Electromagnetic absorbers have wide applicability across the radio frequency (RF) and optical regimes, including such diverse uses as signature control,[1−8] spectroscopy,[9,10] solar cell enhancement,[11,12] thermal imaging,[13−15] and emissivity control.[14,16−18] Among the electromagnetic structures that have been investigated, metamaterials composed of nanoscale resonators with customized electric and/or magnetic response have emerged as compelling candidates for optical wavelength absorbers, with recent efforts focused on mid-infrared (IR) structures having multiband and wide field-of-view (FOV) properties.[18−22] Nearly ideal blackbody absorbers have been demonstrated for the visible and mid-IR spectral regimes using nonresonant nanomaterial structures, including metal-dielectric composites[23] and and vertically aligned single-wall carbon nanotubes.[24] However, these solutions offer limited flexibility to tailor the wavelength range, polarization, and/or angular response of the broadband absorptivity. Metamaterial design approaches can be used to create broadband optical absorbers with such advanced functionalities, but progress toward this goal has been limited by the narrow bandwidth of the individual EM resonator elements and the challenge of impedance matching over a wide spectral range.[25−27]

Electromagnetic absorbers rely on electric or magnetic losses in the constituent material to convert an electromagnetic wave into heat. One promising design approach considers the entire metamaterial to be an effective medium and uses nanoscale resonator elements to introduce large imaginary parts in the effective permittivity and/or permeability dispersion of the homogenized medium.[2,28−31] The imaginary dispersive properties result in high absorption over a narrow band around resonance as the wave passes through the medium. Multiple closely spaced resonances can be realized by incorporating discrete resonators of different sizes into a single unit cell period.[27] The number of different resonator

* Address correspondence to dhw@psu.edu, tsm2@psu.edu.

Received for review November 3, 2013 and accepted January 28, 2014.

**Published online January 28, 2014**
**10.1021/nn4057148**

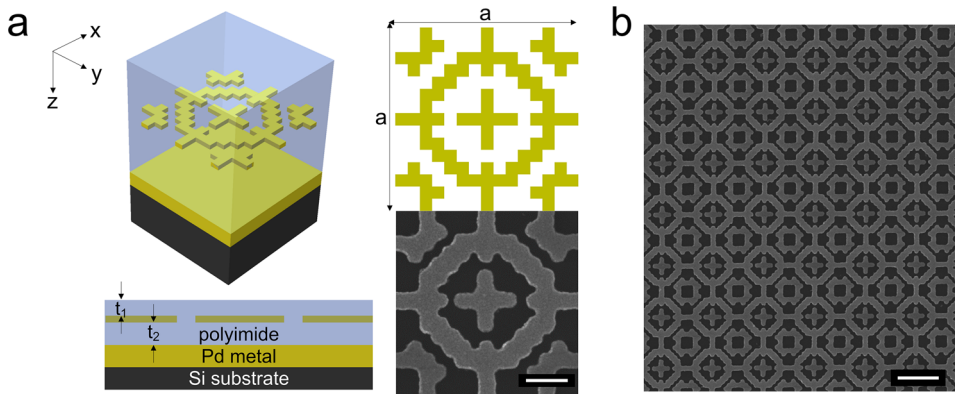


**Figure 1. Diagram and FESEM image of the MMA. (a) Top: Schematic of the Pd-based MMA structure optimized to have broadband absorption from 2 to 5 $\mu$m in the mid-IR. Bottom left: Cross-sectional view of the four-layer EBG-based broadband absorber. Bottom right: FESEM image of one unit cell. Scale bar is 200 nm. (b) Low-magnification FESEM image showing the nanofabricated structure. Scale bar is 600 nm.**

types that can be patterned at dimensions compatible with IR operation is limited, which restricts the absorption bandwidth that can be obtained. It has also been proposed that bandwidth can be increased by integrating many nanoscale resonators into a unit cell by stacking them on top of each other.[32] However, fabricating multiple aligned nanoscale features is complex and time-consuming, and the proposed structures are only strongly absorbing for a single polarization.

Metamaterial absorbers (MMAs) based on electromagnetic band gap (EBG) surfaces offer a compelling alternative with more straightforward nanofabrication. EBG absorbers employ a single lossy metallic screen backed by dielectric and ground layers to form a resonant cavity that couples with incident electromagnetic waves.[1] Narrow single-band and multiband THz and IR EBG MMAs have been demonstrated with near unity absorption, polarization independence, and wide FOV.[19−21,33] Efforts have been made to extend this design concept to create IR absorbers with wide and controlled bandwidths by combining resonators of different sizes in the same metallic screen,[25,26] but achieving high absorption over an octave bandwidth in the IR has so far remained an elusive goal.

In this paper, we report an EBG-based MMA that provides near-ideal spectral absorptivity across a broad mid-IR band with well-defined band edge wavelengths. A genetic algorithm (GA) is employed to identify a single-layer nanostructured metallic screen geometry that supports multiple overlapping resonances to cover greater than an octave bandwidth. A dielectric superstrate layer is introduced to improve the impedance match to free space, thereby minimizing reflectivity and maximizing absorptivity across the band. The traditional gold (Au) metal is replaced by palladium (Pd) to broaden the MMA bandwidth and to improve fabrication reproducibility. Measurements of the optimized EBG-MMA show strong agreement with simulations, demonstrating a 98% average spectral absorptivity over a predefined 1.77 to 4.81 $\mu$m wavelength band and $\pm 45°$ angular range. This work represents a significant step toward realizing practical optical MMAs that provide near-unity broadband absorption over a specified wavelength range, enabling the realization of customized IR black bodies and sources.

## RESULTS AND DISCUSSION

**Electromagnetic Optimization Methodology.** The structure for our broadband EBG-based MMA consists of a four-layer metallodielectric stack, as shown in Figure 1. The bottom three layers of the structure create the resonant electromagnetic cavity of the absorber, which is composed of a doubly periodic array of metal nanostructures patterned on a thin dielectric layer that is backed by a solid metal ground plane. A second dielectric layer is included on top of the structure to provide an impedance match between the metallic nanostructures and free space. This three-layer resonant electromagnetic cavity can be optimized to produce multiple overlapping resonances over a broad bandwidth in the near-to-mid-IR range. In addition, the metal ground plane prevents light transmission through the MMA, thereby causing the incident light to be either reflected or absorbed. At each electric or magnetic resonance, high currents are generated in different regions of the metallic nanostructure array, resulting in strong absorption due to metallic loss.

We employed a robust GA optimizer to identify a metallic nanostructure array that simultaneously maximizes absorption over a broad bandwidth while also giving a wide FOV and polarization-independent response. The GA is a stochastic optimizer that evolves an initial population of randomly generated candidate nanostructures based on the principles of natural selection.[34] Each population member is a binary string, called a chromosome, which contains the encoded design parameters. This optimization approach affords great flexibility to access complex and nonintuitive nanostructure features that fall well outside the

bounds of conventional resonant elements such as crosses and rings.[2,3,9] Our design methodology exploits this flexibility to find elements that can support multiple resonances across the wavelength range of interest, thereby enabling MMAs with extremely wide absorption bandwidths.

In this work, we targeted a MMA with a minimum absorptivity of greater than 90% over an angular range of ±40° and more than an octave of bandwidth across the 2−5 $\mu$m mid-IR spectral range. For this work, structures were optimized using two different noble metals with low reactivity, Au and Pd, for both the ground plane and patterned nanoresonator layer. Polyimide was selected for both dielectric layers because of its nondispersive optical properties over the target wavelength range. Most of the previous single- and multiband mid-IR absorbers were based on Au resonant structures;[19−21,26,33] thus we investigated Au for our broadband MMAs, as well. Recently, a single-band absorber with exposed Pd nanostructures was used for highly sensitive hydrogen gas detection due to the hydrogen absorption properties of Pd metal.[35] Here, we show that the higher optical loss of Pd as compared to the more commonly used Au metal provides significant advantages for robust and reproducible fabrication of broadband EBG-based MMAs. Consequently, the optimized absorber design that satisfied the target properties incorporated Pd rather than Au resonant elements. Our nanofabricated absorbers were characterized in nitrogen ($N_2$), which mitigated optical property changes due to environmental exposure. Practical applications would be enabled by replacing the polyimide layers with an alternate dielectric such as silicon nitride ($Si_3N_4$), which forms an excellent diffusion barrier against hydrogen, oxygen, and moisture.[36] In addition, the costly noble metals used in this work could be replaced with less expensive metals having similar optical properties, such as nickel (Ni) or tungsten (W).

The GA evolved all of the adjustable design parameters within predefined ranges to identify a four-layer MMA that meets the target optical properties, including the thickness of each layer, the unit cell period, and the patterned metal feature geometry. The metal ground plane layer thickness was fixed at 100 nm, which is several times the skin depth for both Pd and Au. The MMA was optimized by encoding one unit cell of the nanostructure array as a 15 × 15 binary grid, where "1" represents a pixel with a metal feature and "0" represents a pixel without a metal feature. The unit cell was forced to have 8-fold mirrored symmetry, which provides polarization independence. This also greatly reduces the computation time required to identify a structure that satisfies the target optical properties because only one triangular fold must be optimized by the GA.

In each optimization cycle, the optical properties of all candidate MMA unit cells in the population were evaluated with a full-wave electromagnetic solver and compared to the target properties. More specifically, we calculated the reflectance and transmittance at a set of test wavelengths and angles using a full-wave finite-element boundary integral (FEBI) technique.[37] Because the metal ground layer is thick enough to fully attenuate the wave, the transmittance is zero and the absorptivity is the difference between unity and the reflectance. The deviation between the properties of the candidate unit cell and the target is evaluated according to the following *cost* function:

$$\text{cost} = \sum_{\lambda_i}\sum_{(\theta,\phi)_j} (1.0 - A_{TE})^2 + (1.0 - A_{TM})^2 \qquad (1)$$

where $A_{TE}$ and $A_{TM}$ are the transverse electric (TE) and transverse magnetic (TM)-polarized absorptivities, $\lambda_i$ are the test wavelengths, and $(\theta,\varphi)_j$ are the test incidence angles. By minimizing the cost function in eq 1, the GA evolves the nanostructure pattern and layer thicknesses that have near unity absorption over all of the test wavelengths and incidence angles. For this specific mid-IR broadband MMA design, we specified 16 test wavelengths in approximately equally spaced frequency intervals over the range from 2 to 5 $\mu$m. The test incidence angles were chosen to be $(\theta,\varphi)_i$ = {(0°,0°), (40°,0°), (40°,45°)}, covering a FOV up to ±40°. Throughout the evolutionary process, structures that failed to meet predefined nanofabrication constraints were assigned a high cost and were eliminated from subsequent candidate populations.[38] This ensured that the optimized structure could be fabricated without changes, which is essential for subsequent experimental verification of the broadband MMA response. Using a population of 24 chromosomes, the GA converged to a structure with minimized cost in 86 generations.

**Subwavelength Nanostructure Array for Broadband Absorption.** An illustration of the GA-optimized broadband MMA and a detailed diagram of the metallic nanostructure unit cell are displayed in Figure 1a. The optimized thicknesses are $t_1$ = 398 nm and $t_2$ = 429 nm for the top and bottom polyimide layers and 30 nm for the patterned Pd nanostructures. The unit cell period is $a$ = 851 nm with a pixel size of 57 nm. Three well-defined nanostructures, which obey the predefined fabrication constraints, are noted: (1) a cross dipole centered in the unit cell; (2) a large loop centered in the unit cell and interconnected between unit cells; and (3) four smaller, isolated loops centered at the corners of the unit cell. These nanostructure elements and the coupling between them support multiple electromagnetic resonances with narrowly spaced center wavelengths, which produce high absorption across the broad mid-IR band.

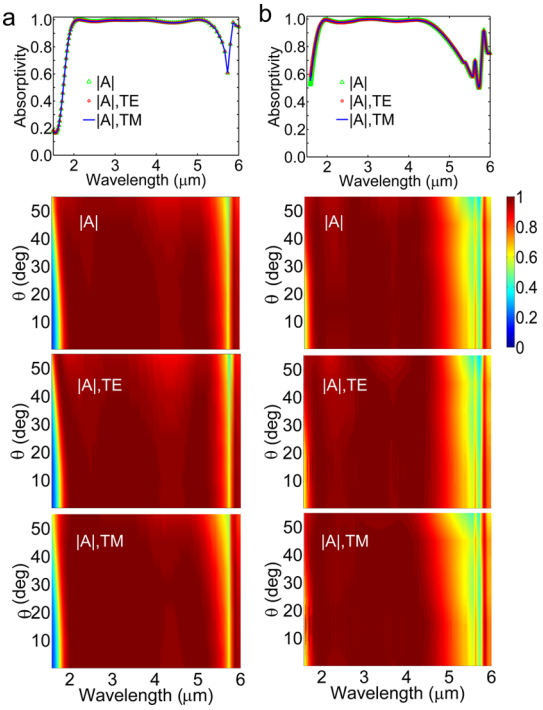


**Figure 2. Angular dispersion of the MMA absorption spectra. (a) Simulated and (b) measured absorptivity of the design from Figure 1. Top row: Normal incidence absorptivity for unpolarized, TE, and TM illumination. Contour plot of absorptivity as a function of wavelength and incident angle from normal up to 55° under unpolarized (second row), TE (third row), and TM (bottom row) illumination.**

The simulated absorptivity of the MMA calculated from the scattering parameters by $A = 1 - R$, where $R$ is the reflectance, is shown Figure 2a for unpolarized, TE-polarized, and TM-polarized light (see Methods for a detailed description of the electromagnetic simulation approach). The normal incidence spectra in Figure 2a demonstrate that the minimum spectral absorptivity for this structure is greater than 90% over the entire 1.90 to 5.47 $\mu$m range, achieving a high average value of 98.8% across this band. It is evident from these spectra that the broadband absorption is due to the convolution of multiple strong resonances positioned at optimized wavelengths across the band; the peak values of absorptivity at normal incidence occur at 2.13, 3.00, 3.70, and 5.05 $\mu$m. Figure 2a shows 2D contour plots of the predicted angular dependence of the absorptivity from normal $\theta = 0°$ up to $\theta = 55°$ off-normal incidence for all polarizations. Individual off-normal curves plotted in increments of 10° are provided from $\theta = 0°$ to $\theta = 55°$ in Supporting Information, Figures S1 and S2. These simulations reveal that more than an octave bandwidth with minimum absorptivity of 89.5% and an average absorptivity of 94.7% is maintained over the 2−5 $\mu$m band at an incidence angle of $\theta = 55°$, which is wider than the targeted FOV used for optimization. Comparing the TE and TM responses, we note that the TM absorption at 5 $\mu$m drops off more quickly with increasing incidence angle as compared with the TE-polarized response, whereas the dip in absorptivity around 4.5 $\mu$m becomes more pronounced for the TE polarization at large incidence angles. These small changes in MMA response with increasing incidence angle are associated with slight shifts in peak position, strength, and bandwidth of the dominant resonances found at normal incidence. Finally, the plots in Figure S2 also show that high average absorptivity around 72.6% is maintained over an octave of bandwidth all the way to $\theta = 75°$, with absorptivity dropping off quickly as the angle approaches grazing incidence.

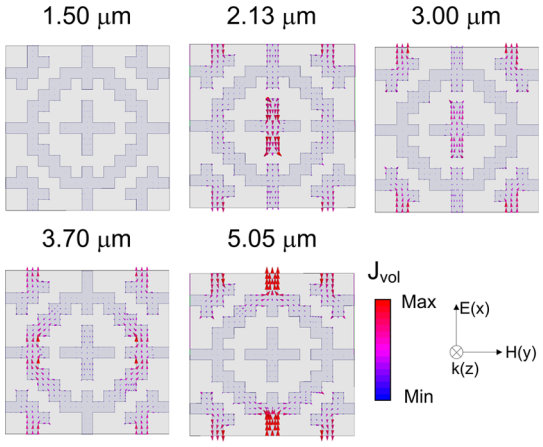


**Figure 3. Top view of finite-element method simulations of the current distributions in the top Pd screen for normal incidence at out of band and peak wavelengths of 1.50, 2.13, 3.00, 3.70, and 5.05 $\mu$m.**

**Resonant Electromagnetic Properties.** To understand the contribution of the different subwavelength nanostructures to the broadband absorption, the electric volume currents excited within the MMA were simulated for normally incident, TE-polarized illumination in the mid-IR range.[21] Figure 3 shows top views of the current distribution for TE-polarized illumination at resonant wavelengths within the band where absorption is highest (2.13, 3.00, 3.70, and 5.05 $\mu$m) and at one wavelength outside the band (1.50 $\mu$m) where reflection dominates. Cross-sectional views of the current and the electric field distribution are shown in Supporting Information, Figures S3 and S4. Outside the absorption band at 1.50 $\mu$m, the electric current in the MMA is negligible, and only a small field enhancement is observed from the standing wave that is terminated at the metal ground plane. In contrast, large electric currents and field enhancements are found on different parts of the Pd nanostructure array at wavelengths corresponding to peak in-band absorption. Specifically, the central crosses support the highest current at the shortest 2.13 $\mu$m wavelength. The current distribution spreads from the central cross to include the large and small loops at the intermediate 3.00 and 3.70 $\mu$m wavelengths. At the longest 5.05 $\mu$m wavelength, the

electric current is high on all parts of the nanostructure except the central cross.

Compared to other MMAs that excite magnetic resonances,[21] the strong broadband absorption in this MMA is entirely due to electric resonances. The side views of the electric volume currents in Figure S3 show that large currents are only present on the Pd nanostructure layer and not on the ground plane. This occurs because the relatively thick polyimide substrate layer prevents strong coupling between the patterned nanostructure and the ground layer, which inhibits loop currents associated with a magnetic response. These simulation results demonstrate that the broadband performance of this mid-IR EBG-MMA is achieved by exciting multiple closely wavelength-spaced electric resonances on the single-layer nanostructure array.

**Nanofabrication and Optical Measurements.** The optimized MMA was fabricated by first evaporating the Pd ground plane layer and spin coating the polyimide substrate layer on a Si handle wafer. Next, the doubly periodic Pd nanostructure array (3 mm × 3 mm) was patterned on top of the polyimide layer using electron-beam lithography followed by a Pd lift-off process. The MMA was completed by spin coating the polyimide superstrate layer (see Methods for a detailed description of the process parameters). Field emission scanning electron microscope (FESEM) images taken immediately after the Pd nanostructures were defined on the polyimide substrate are shown in Figure 1b. These images confirm that the complex array features were reproduced in the fabricated MMA sample. The measured unit cell period of $a$ = 860 nm closely matched the target $a$ = 851 nm. In comparison to the square 57 nm pixels in the design, the fabricated Pd nanostructures had rounded edges, with a central dimension of ~75 nm. Although this process is compatible with creating a flexible MMA conformable to curved surfaces,[21] our structure was left on the handle wafer for optical characterization.

The reflectance of the fabricated MMA was measured using a Fourier transform infrared (FTIR) spectrometer at angles of incidence between 0 and 55° off-normal (see Methods for a description of the measurement setup). The normal incidence absorptivity determined from $A = 1 - R$ and plotted in Figure 2b shows that minimum absorption remains above 90% independent of polarization at wavelengths between 1.77 and 4.81 $\mu$m (greater than an octave bandwidth), with an average absorption of 98.1% over this same range. Compared to the full-wave simulation, the bandwidth is reduced from 3.57 to 3.04 $\mu$m primarily because of the blue shift in the long-wavelength band edge from 5.47 to 4.81 $\mu$m. This is associated with a reduction in the number of absorption maxima from four to three and a shift in the peaks to 1.97, 3.09, and 4.23 $\mu$m. Figure 2b displays 2D contour plots of the measured oblique incidence absorptivity for TE, TM, and unpolarized light, with the corresponding curves plotted in 10° increments provided in Supporting Information, Figure S1. These plots show that a full octave of bandwidth with higher than 90% absorptivity is maintained all the way out to incident angles of 55°. In addition, the trends in the angular dependence of the polarized response follow theoretical predictions.

These results demonstrate that the nanofabricated broadband MMA achieves the high and wide FOV in-band absorption expected from simulation of the ideal optimized structure. The primary discrepancy between experiment and theory is the shift in the long-wavelength response, which results in a slight reduction in the bandwidth of the structure. The potential sources of this discrepancy include (1) an increase in the Pd nanostructure feature size; (2) error in the polyimide superstrate and substrate thickness; and (3) differences in the dispersive properties ($n$ and $k$) of the evaporated Pd film following thermal processing. To determine the most likely causes, we resimulated the optical response of the MMA using the fabricated Pd nanostructure feature dimensions as well as different polyimide thicknesses (see Supporting Information, Figure S5). These simulations reveal that the feature size modifies the response of the central resonances but has little impact on the short- or long-wavelength response. In contrast, decreasing both the superstrate and substrate polyimide thicknesses by only 10% provides a match to the short-wavelength band edge and better agreement with the long-wavelength band edge. Therefore, we believe that the discrepancy is largely due to errors in the polyimide thickness combined with small changes in the thermally processed Pd optical constants. We expect that further refinement of the nanofabrication process would result in a structure with even closer agreement to theory.

**Selection of Metal for Broadband Absorption.** During this work, we also evaluated the trade-offs of using Au *versus* Pd metal for the nanostructure array and ground layers in the four-layer broadband MMA. Figure 4 shows a Au-based broadband MMA that was optimized using the cost function given in eq 1. Similar to the optimized Pd-based MMA, the simulated response plotted in Figure 4c shows that this design can achieve greater than 90% absorptivity over a broad band from 2 to 5 $\mu$m and a wide FOV of ±40°. The optimized thicknesses are $t_1$ = 423 nm and $t_2$ = 456 nm for the polyimide superstrate and substrate layers and 10 nm for the patterned Au nanostructures. The unit cell period is $a$ = 998 nm with a pixel size of 67 nm. Because Au is more conductive than Pd in the mid-IR, the optimized Au nanostructure film thickness that provides a good impedance match over such a large bandwidth is only 10 nm as compared to 30 nm for the Pd nanostructure films. This makes the optical properties of the Au-based MMA more sensitive to small variations in metal thickness.

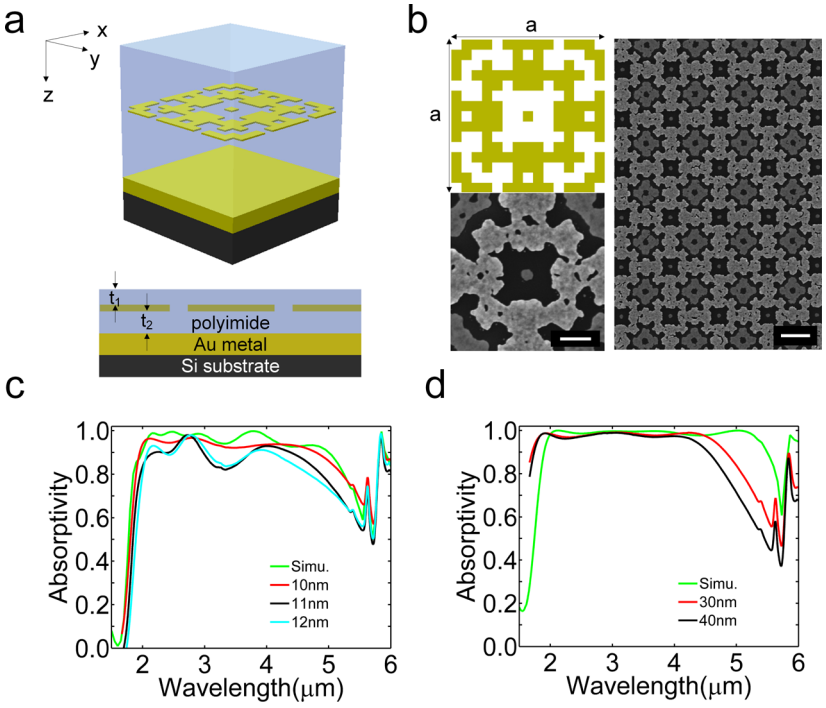


**Figure 4. (a) Diagram of the optimized Au-based MMA structure. (b) Top left: Top view of one unit cell of the design. Bottom left: FESEM image of a unit cell of the fabricated structure. Scale bar is 200 nm. Right: Low-magnification FESEM image of the same structure. Scale bar is 600 nm. (c) Simulation and measurements for Au-based MMA under unpolarized illumination at normal incidence. The average Au thicknesses of the Au nanostructures determined by atomic force microscopy measurements are 10, 11, and 12 nm. (d) Simulation and measurements for Pd-based MMAs with Pd nanostructure thicknesses of 30 and 40 nm under unpolarized illumination at normal incidence.**

To investigate this Au-based structure experimentally, we fabricated the optimized MMA shown in Figure 4a,b with average Au nanostructure film thicknesses that varied from 10 to 12 nm in increments of ~1 nm (see Methods for a detailed description of the process parameters). The measured absorptivity of the three fabricated MMAs is compared to simulation in Figure 4c. The MMA with the 10 nm thick Au features maintains a high absorptivity greater than 90% over a broadband between 1.95 and 4.80 $\mu$m. However, the structure has a lower average broadband absorptivity of 94.4% as compared to that of the optimized Pd-based MMA. Increasing the Au film thickness to 11 and 12 nm results in large fluctuations in spectral absorptivity and a reduction in absorption near the long-wavelength band edge, giving a lower average absorptivity of 89.2% across the band. To determine the sensitivity of the MMA to small variations in the Au film thickness, we resimulated its optical response for Au nanostructure film thicknesses ranging from 10 to 14 nm in increments of 1 nm (see Supporting Information, Figure S6). These simulations verify the trends observed in the experimental measurements. In contrast, the absorptivity of the optimized Pd-based MMA is relativity insensitive to Pd thickness, as shown in Figure 4d. In this case, an increase in Pd thickness from 30 to 40 nm had a negligible effect on the absorption with only a slight reduction in the long-wavelength band edge from 4.81 to 4.48 $\mu$m. This underscores the importance of identifying constituent materials and nanostructure geometries that are robust against process variations for high-performance metamaterial designs.

## CONCLUSIONS

This paper reported a polarization-independent metallodielectric EBG-based MMA with an average absorptivity of 98% over greater than an octave bandwidth from 1.77 to 4.81 $\mu$m and a wide $\pm$45° FOV. A robust GA design approach was employed to identify a doubly periodic metal nanostructure array that excites multiple closely spaced electric resonances for the broad absorption band. The optimized unit cell of the nanostructure array integrates three well-defined electromagnetic elements in a single metal screen layer that meets predefined fabrication constraints. Simulations showed that the incident light induces large electric currents and field enhancements on different parts of the metal nanostructure at wavelengths corresponding to peak in-band absorption, thereby confirming the importance of each of these elements as well as the coupling between them to the high absorption. Comparing designs optimizing using Au and Pd nanostructures reveals that Pd improves the broadband optical properties and fabrication reproducibility. This demonstration confirms that a single-layer metal nanostructure array can produce nearly ideal

broadband absorption with well-controlled band edge wavelengths, paving the way for a variety of highly customizable optical metamaterial absorbers with superoctave bandwidth.

## METHODS

**Metamaterial Absorber Electromagnetic Simulation.** The scattering parameters of the optimized MMAs were calculated using the Ansoft High Frequency Structure Simulator (HFSS) full-wave finite-element solver. Periodic boundary conditions were applied to a single unit cell, which was excited by a plane wave. The measured dispersive optical properties of polyimide, Pd, and Au were included in the model.

**Broadband Metamaterial Absorber Nanofabrication and Characterization.** Nanofabrication of the MMA began by depositing 100 nm Pd and 10 nm Ti on a Si wafer by electron-beam evaporation (Kurt J Lesker Lab18) at a rate of 1.4 Å/s. The 429 nm thick dielectric substrate layer was prepared by spin coating the polyimide precursor (HD Microsystems PI2556 diluted with T9039 thinner) at 1850 rpm for 40 s and soft baking at 120 °C for 1 min. The film was cured in a $N_2$-purged oven for 2 h at 220 °C to fully remove the solvent and imidize the dielectric film. Following this step, the electron-beam resist (Nippon ZEP520A) diluted with anisole 1:1 was spun on the substrate at 3000 rpm for 50 s and baked at 180 °C for 3 min. The single-layer nanostructure array was defined by electron-beam lithography (Vistec EBPG 5200) at a dose of 270 $\mu$C/cm$^2$ and developed using *n*-amyl acetate for 3 min and MIBK/IPA = 8:1 for 1 min. The top 30 nm Pd was evaporated with a deposition rate of 1 Å/s and lifted-off by dissolving the resist (Rohm & Haas Microposit Remover 1165). The 398 nm thick dielectric superstrate layer was deposited by spinning the polyimide precursor at 2100 rpm for 40 s. The film was soft baked and cured using the same conditions as the substrate layer. The Au-based MMAs were fabricated using the same process flow. For these structures, the top 10 to 12 nm thick Au films were deposited at a rate of 0.5 Å/s. The thicknesses of the patterned Pd and Au nanostructures were measured by atomic force microscopy (AFM) before depositing the top polyimide layer (AFM, Bruker Icon). For the thinnest Au films that were not continuous, the effective film thickness was estimated by averaging AFM height measurements from at least five different locations on the sample.

The optical properties of all of the constituent materials used for GA optimization and electromagnetic simulation were characterized by variable-angle spectroscopic ellipsometry (J.A. Woollam IR-VASE). The 3 mm × 3 mm EBG-MMA was characterized using a $N_2$-purged FTIR spectrometer (Bruker Optics IFS-66) equipped with a liquid-nitrogen-cooled mercury cadmium telluride detector. A custom-designed setup was used for normal incidence reflection measurements. The oblique incidence measurements were made using a specular reflection accessory (Thermo Spectra-tech model 500). The measured reflectance was referenced to a Au mirror to determine the absolute reflectivity, *R*. The absorptivity was determined according to $A = 1 - R - T$, where $T = 0$.

*Conflict of Interest:* The authors declare no competing financial interest.

*Acknowledgment.* The authors acknowledge support from the NSF MRSEC Grant No. DMR-0213623. L.L. acknowledges additional support from NSF Grant No. DMR-1125591. The MMAs were fabricated at the Penn State NSF NNIN Site.

*Supporting Information Available:* FTIR measurement and simulation of MMA with curves for off-normal angles; simulations of the MMA in Figure 1 showing off-normal performance up to grazing incidence; side view of the current distributions in the MMA in Figure 1; simulations of the electric field enhancement in the MMA in Figure 1; geometry and simulated absorptivity of the nanofabricated MMA in Figure 1; simulations of the absorptivity of the Au-based MMA in Figure 4 for varying Au nanostructure thicknesses. This material is available free of charge *via* the Internet at http://pubs.acs.org.

## REFERENCES AND NOTES

1. Kern, D. J.; Werner, D. H. A Genetic Algorithm Approach to the Design of Ultra-thin Electromagnetic Bandgap Absorbers. *Micro. Opt. Technol. Lett.* **2003**, *38*, 61–64.
2. Landy, N. I.; Sajuyigbe, S.; Mock, J. J.; Smith, D. R.; Padilla, W. J. A Perfect Metamaterial Absorber. *Phys. Rev. Lett.* **2008**, *100*, 207402.
3. Wan, B.; Koschny, T.; Soukoulis, C. M. Wide-Angle and Polarization-Independent Chiral Metamaterial Absorber. *Phys. Rev. B* **2009**, *80*, 033108.
4. Cheng, Q.; Cui, T. J.; Jiang, W. X.; Cai, B. G. An Omnidirectional Electromagnetic Absorber Made of Metamaterials. *New J. Phys.* **2010**, *12*, 063006.
5. Hutley, M. C.; Maystre, D. The Total Absorption of Light by a Diffraction Grating. *Opt. Commun.* **1976**, *19*, 431–436.
6. Bonod, N.; Tayeb, G.; Maystre, D.; Enoch, S.; Popov, E. Total Absorption of Light by Lamellar Metallic Gratings. *Opt. Express* **2008**, *16*, 15431.
7. Le Perchec, J.; Quémerais, P.; Barbara, A.; López-Ríos, T. Why Metallic Surfaces with Grooves a Few Nanometers Deep and Wide May Strongly Absorb Visible Light. *Phys. Rev. Lett.* **2008**, *100*, 066408.
8. Narimanov, E. E.; Kildishev, A. V. Optical Black Hole: Broadband Omnidirectional Light Absorber. *Appl. Phys. Lett.* **2009**, *95*, 041106.
9. Tao, H.; Bingham, C. M.; Strikwerda, A. C.; Pilon, D.; Shrekenhamer, D.; Landy, N. I.; Fan, K.; Zhang, X.; Padilla, W. J.; Averitt, R. D. Highly Flexible Wide Angle of Incidence Terahertz Metamaterial Absorbers: Design, Fabrication, and Characterization. *Phys. Rev. B* **2008**, *78*, 241103.
10. Zhu, W.; Zhao, X. Metamaterial Absorber with Dendritic Cells at Infrared Frequencies. *J. Opt. Soc. Am. B* **2009**, *26*, 2382–2385.
11. Wang, C.; Yu, S.; Chen, W.; Sun, C. Highly Efficient Light-Trapping Structure Design Inspired by Natural Evolution. *Sci. Rep.* **2013**, *3*, 1025.
12. Teperik, T. V.; García de Abajo, F. J.; Borisov, A. G.; Abdelsalam, M.; Bartlett, P. N.; Sugawara, Y.; Boumberg, J. J. Omnidirectional Absorption in Nanostructured Metal Surfaces. *Nat. Photonics* **2008**, *2*, 299–301.
13. Landy, N. I.; Bingham, C. M.; Tyler, T.; Jokerst, N.; Smith, D. R.; Padilla, W. J. Design, Theory, and Measurement of Polarization-Insensitive Absorber for Terahertz Imaging. *Phys. Rev. B* **2009**, *79*, 125104.
14. Diem, M.; Koschny, T.; Soukoulis, C. M. Wide-Angle Perfect Absorber/Thermal Emitter in the Terahertz Regime. *Phys. Rev. B* **2009**, *79*, 033101.
15. Hibbins, A. P.; Murray, W. A.; Tyler, J.; Wedge, S.; Barnes, W. L.; Sambles, J. R. Resonant Absorption of Electromagnetic Fields by Surface Plasmons Buried in a Multilayered Plasmonic Nanostructure. *Phys. Rev. B* **2006**, *74*, 073408.
16. Bossard, J. A.; Werner, D. H. Metamaterials with Angle Selective Emissivity in the Near-Infrared. *Opt. Express* **2013**, *21*, 5215–5225.
17. Bossard, J. A.; Werner, D. H. Metamaterials with Custom Emissivity Polarization in the Near-Infrared. *Opt. Express* **2013**, *21*, 3872–3884.
18. Liu, X.; Tyler, T.; Starr, T.; Starr, A. F.; Jokerst, N. M.; Padilla, W. J. Taming the Blackbody with Infrared Metamaterials as Selective Thermal Emitters. *Phys. Rev. Lett.* **2011**, *107*, 045901.
19. Zhang, B.; Zhao, Y.; Hao, Q.; Kiraly, B.; Khoo, I.-C.; Chen, S.; Huang, T. J. Polarization-Independent Dual-Band Infrared Perfect Absorber Based on a Metal-Dielectric-Metal Elliptical Nanodisk Array. *Opt. Express* **2011**, *19*, 15221.
20. Liu, N.; Mesh, M.; Weiss, T.; Hentschel, M.; Giessen, H. Infrared Perfect Absorber and Its Application as Plasmonic Sensor. *Nano Lett.* **2010**, *10*, 2342–2348.

21. Jiang, Z. H.; Yun, S.; Toor, F.; Werner, D. H.; Mayer, T. S. Conformal Dual-Band Near-Perfectly Absorbing Mid-infrared Metamaterial Coating. *ACS Nano* **2011**, *5*, 4641–4647.
22. Dayal, G.; Ramakrishna, S. A. Design of Multi-band Metamaterial Perfect Absorbers with Stacked Metal-Dielectric Disks. *J. Opt.* **2013**, *15*, 055106.
23. Hedayati, M. K.; Javaherirahim, M.; Mozooni, B.; Abdelaziz, R.; Tavassolizadeh, A.; Chakravadhanula, V. S. K.; Zaporojtchenko, V.; Strunkus, T.; Faupel, F.; Elbahri, M. Design of a Perfect Black Absorber at Visible Frequencies Using Plasmonic Metamaterials. *Adv. Mater.* **2011**, *23*, 5410–5414.
24. Mizuno, K.; Ishii, J.; Kishida, H.; Hayamizu, Y.; Yasuda, S.; Futaba, D. N.; Yumura, M.; Hata, K. A Black Body Absorber from Vertically Aligned Single-Walled Carbon Nanotubes. *Proc. Natl. Acad. Sci. U.S.A.* **2009**, *106*, 6044–6047.
25. Aydin, K.; Ferry, V. E.; Briggs, R. M.; Atwater, H. A. Broadband Polarization-Independent Resonant Light Absorption Using Ultrathin Plasmonic Super Absorbers. *Nat. Commun.* **2011**, *2*, 1528.
26. Cui, Y.; Xu, J.; Fung, K. H.; Jin, Y.; Kumar, A.; He, S. A Thin Film Broadband Absorber Based on Multi-sized Nanoantennas. *Appl. Phys. Lett.* **2011**, *99*, 253101.
27. Luo, H.; Wang, T.; Gong, R.-Z.; Nie, N.; Wang, X. Extending the Bandwidth of Electric Ring Resonator Metamaterial Absorber. *Chin. Phys. Lett.* **2011**, *28*, 034204.
28. Avitzour, Y.; Urzhumov, Y. A.; Shvets, G. Wide-Angle Infrared Absorber Based on a Negative-Index Plasmonic Metamaterial. *Phys. Rev. B* **2009**, *79*, 045131.
29. Tao, H.; Landy, N. I.; Binham, C. M.; Zhang, X.; Averitt, R. D.; Padilla, W. J. A Metamaterial Absorber for the Terahertz Regime: Design, Fabrication and Characterization. *Opt. Express* **2008**, *16*, 7181–7188.
30. Bayraktar, Z.; Gregory, M. D.; Wang, X.; Werner, D. H. Matched Impedance Thin Planar Composite Magneto-Dielectric Metasurfaces. *IEEE Trans. Antennas Propag.* **2012**, *60*, 1910–1920.
31. Werner, D. H.; Bossard, J. A.; Bayraktar, Z.; Zhang, Z. H.; Gregory, M. D.; Werner, P. L. Nature Inspired Optimization Techniques for Metamaterial Design. In *Numerical Methods for Metamaterial Design*; Diest, K., Ed.; Springer: Heidelberg, Germany, 2013; pp 97−146.
32. Cui, Y.; Fung, K. H.; Xu, J.; Ma, H.; Jin, Y.; He, S.; Fang, N. X. Ultrabroadband Light Absorption by a Sawtooth Anisotropic Metamaterial Slab. *Nano Lett.* **2012**, *12*, 1443–1447.
33. Liu, X.; Starr, T.; Starr, A. F.; Padilla, W. J. Infrared Spatial and Frequency Selective Metamaterial with Near-Unity Absorbance. *Phys. Rev. Lett.* **2010**, *104*, 207403.
34. Haupt, R. L.; Werner, D. H. *Genetic Algorithms in Electromagnetics*; Wiley: Hoboken, NJ, 2007.
35. Tittl, A.; Mai, P.; Taubert, R.; Dregely, D.; Liu, N.; Giessen, H. Palladium-Based Plasmonic Perfect Absorber in the Visible Wavelength Range and its Application to Hydrogen Sensing. *Nano Lett.* **2011**, *11*, 4366–4369.
36. Plummer, J. D.; Deal, M.; Griffin, P. D. *Silicon VLSI Technology: Fundamental, Practice, and Modeling*; Prentice Hall: Upper Saddle River, NJ, 2000.
37. Eibert, T. F.; Volakis, J. L.; Wilton, D. R.; Jackson, D. R. Hybrid FE/BI Modeling of 3-D Doubly Periodic Structures Utilizing Triangular Prismatic Elements and an MPIE Formulation Accelerated by the Ewald Transformation. *IEEE Trans. Antennas Propag.* **1999**, *47*, 843–850.
38. Tang, Y.; Bossard, J. A.; Werner, D. H.; Mayer, T. S. Single-Layer Metallodielectric Nanostructures as Dual-Band Mid-infrared Filters. *Appl. Phys. Lett.* **2008**, *92*, 263106.